

# Delocalization Transition in Colloidal Crystals

Hector Lopez-Rios,<sup>†,¶</sup> Ali Ehlen,<sup>‡,¶</sup> and Monica Olvera de la Cruz<sup>\*,†,‡</sup>

<sup>†</sup>*Department of Materials Science and Engineering, Northwestern University*

<sup>‡</sup>*Applied Physics Program, Northwestern University*

<sup>¶</sup>*Equal contribution*

E-mail: m-olvera@northwestern.edu

Phone: +1 (847) 491-7801

## Abstract

Sublattice melting is the loss of order of one lattice component in binary or ternary ionic crystals upon increase in temperature. A related transition has been predicted in colloidal crystals. To understand the nature of this transition, we study delocalization in self-assembled, size-asymmetric binary colloidal crystals using a generalized molecular dynamics model. Focusing on BCC lattices, we observe a smooth change from localized to delocalized interstitial particles for a variety of interaction strengths. Thermodynamic arguments, mainly the absence of a discontinuity in the heat capacity, suggest that the passage from localized to delocalized is continuous and not a phase transition. This change is enhanced by lattice vibrations and the temperature of the onset of delocalization can be tuned by the strength of the interaction between the colloid species. Therefore, the localized and delocalized regimes of the sublattice is seen as a competition between enthalpic and entropic driving forces, respectively. This work sets the stage for future studies of sublattice melting in colloidal systems with different stoichiometries and lattice types, and it provides insights into superionic materials, with potential for application in energy storage technologies.

## Introduction

Binary colloidal systems, which have interspecies attraction and intraspecies repulsion, have been shown to self-assemble into a wide variety of binary lattices.<sup>1-5</sup> Generally, if the two colloid species are of sufficiently different sizes, the larger colloids will form a lattice while the smaller colloids occupy interstitial sites.<sup>6-9</sup> In these size-asymmetric colloidal systems, many cubic and non-cubic crystals have been detected, including a Frank-Kasper phase.<sup>9</sup> However, under certain conditions, the small particles may delocalize and roam around the crystal while the large particles remain in lattice sites; this is called sublattice melting. Previously, this behavior had been seen primarily in atomic systems (in materials termed superionics,<sup>10-12</sup>) but recent work has demonstrated sublattice melting in hard spheres under pressure,<sup>7</sup> oppositely charged colloids with a Debye-Hückle potential,<sup>13</sup> and size-asymmetric binary colloidal crystals functionalized with sticky DNA chains.<sup>9</sup> The surprising loss of order of only the sublattice also resembles behavior found in metals. In this analogy, the small particles map to delocalized electrons and the large particles to fixed nuclei. Given the unique physical nature of these colloidal crystals that exhibit sublattice melting, we seek to understand the origin of the sublattice melting using a generalized molecular dynamics (MD) model, which can provide insight into a range of systems.

To calculate reliable thermodynamic and physical quantities of delocalized systems, we developed a scalable MD model. This simplified model enables us to generalize previous work that predicted delocalization in systems of DNA-functionalized gold nanoparticles,<sup>9</sup> where the interactions between colloid species were due to DNA hybridization, which is directional and specific. However, the experimental design also included additional free DNA chains that may have acted as depletants. By avoiding complications dealing with DNA hybridization and to explore the generality of the phenomenon, the interactions in our model are general, isotropic, and short-range. The use of these simple potentials can tell us whether directionality and specificity are important for delocalization. With this model, we can start to address questions that have been posed about the analogous transition

observed in superionic materials<sup>14,15</sup> such as the origin of the sublattice melting transition. We note that contrary to superionics, this model is not constrained by a requirement of charge neutrality per unit cell.

The generality of this model enables us to apply it to a wide variety of colloidal systems. This encompasses, for example, nanodots with thiols and end terminal attractive groups,<sup>16,17</sup> functionalized nanoparticles with light activated interactions,<sup>18,19</sup> and nano-composite tectons.<sup>20–22</sup> In fact, nano-composite tectons would be an ideal system for experimental verification of this study, because the parameters of the system reported in the present work can correspond to metallic nanoparticles functionalized with hydrocarbon chains with short ranged and strong complementary molecular binding pairs.

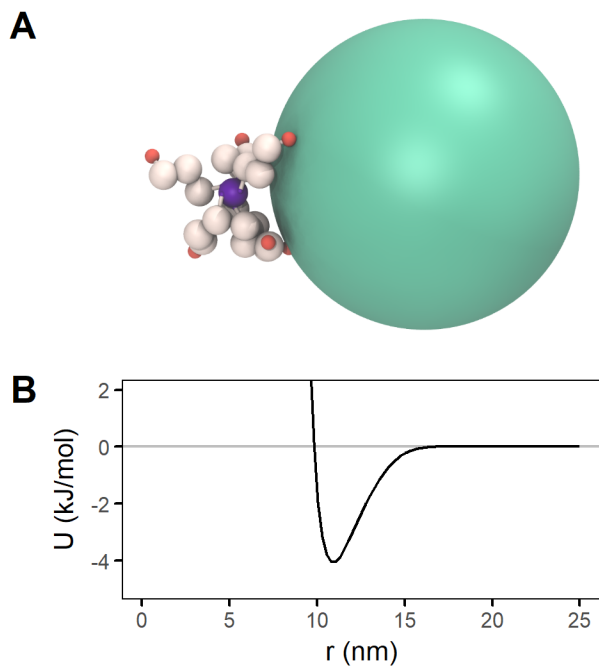


**Figure 1:** The simplified model. **(A)** The smaller colloid (purple) functionalized with chains (white) and larger colloid (turquoise) in our system, to scale. All beads have excluded volume based on their radii, and there is an attractive interaction between the large particles and the interactive ends of the small particle chains (orange). **(B)** Pair potential  $U(r)$  between the centers of the large particles and the interactive chain ends. The high-energy region  $r < 10$  nm represents excluded volume and the small potential well accounts for their attractive interaction. The value of  $U$  at the minimum is -4.1 kJ/mol

An image of the model is shown in Figure 1A. The larger colloidal species is represented

by a single sphere (shown in turquoise). The smaller species is represented by a small sphere (shown in purple) grafted with a variable number of self-avoiding chains (shown in white). The only interactions in the system are excluded volume between all beads, using a Weeks-Chandler-Andersen (WCA) potential, and a generalized, attractive potential between the interactive ends of the chains (shown in orange, referred to here as "interactive ends") and the large particles; see Figure 1B. We chose to further simplify the system by representing the large species as spheres without explicit functionalized chains. However, the smaller colloids' chains must be represented explicitly because their small radius limits the number of chains that can be grafted and therefore allows chains more degrees of freedom, which is important in these systems. We find that an asymmetry of interaction ranges between the large and small particles is needed for delocalization to occur. The range of the attractive potential is half of that of the diameter of the large particles, which are repulsive among themselves, as stated, through a WCA potential.

In this paper, we focus on the localized-to-delocalized transition in colloidal systems containing six small particles for every one large particle (referred to as a 6:1 ratio). We study this transition with respect to temperature and under varying interaction strengths, which we achieve by varying the number of chains on each small colloid. We consider small particles grafted with 4, 6, 8 and 10 chains, respectively. For these parameters, the system is stable as a BCC lattice for a wide range of temperatures. Therefore, with this model we can study the origin and nature of the transition without added complexity of a change of symmetry. We find that both size and interaction strength asymmetries are needed for delocalization to occur. The passage from localized to delocalized is fully continuous, closely related to diffusion of the small particles, and enhanced by vibrational entropy of the large particle lattice. This continuous behavior arises from a competition between enthalpic and entropic driving forces. Here enthalpic contributions can be understood through analysis of the interaction energy landscape between the large particles and interactive beads of the small particles. Entropic contributions arise from the vibrations of the large particle lattice.

The paper is organized as follows. We begin with descriptions and parameters of the MD simulations and the theoretical model used for the free energy analysis of these crystals. We continue with a symmetry and energetic analysis of relevant aspects of a BCC sublattice while introducing the energy landscape for this system. We follow up with an analysis of the evolution of thermodynamic and physical properties such as lattice parameter and specific heat per particle as a function of temperature. We conclude with the importance of lattice vibrations as the driving force for delocalization and lattice expansion for these crystals.

## Methods

### General description of the MD model

The interactions between the beads in the system are simple: all beads have excluded volume interactions with each other through the Weeks-Chandler Anderson (WCA) potential. In addition to this, there is an attractive interaction between the interactive end of the chain and the large particles. That interaction is in the form of a Gaussian potential and is graphically shown in Figure 1B and mathematically here:

$$U_{\text{int}}(r) = \begin{cases} U_{\text{WCA}}(r) + U_{\text{Gaussian}}(r) & r \leq r_{\text{cutoff}} \\ 0 & \text{otherwise} \end{cases} \quad (1)$$

where

$$U_{\text{WCA}}(r) = 4 \left( \left( \frac{\sigma}{r} \right)^{12} - \left( \frac{\sigma}{r} \right)^6 \right) - 4 \left( \left( \frac{\sigma}{2^{1/6}\sigma} \right)^{12} - \left( \frac{\sigma}{2^{1/6}\sigma} \right)^6 \right) \quad \text{for } r \leq 2^{1/6}\sigma \quad (2)$$

$$U_{\text{Gauss}}(r) = -\varepsilon e^{-\frac{1}{2} \left( \frac{r}{\sigma_{\text{gauss}}} \right)^2} \quad \text{for } r \leq r_{\text{cutoff}} \quad (3)$$

where  $r$  is the distance between the centers of the large particle and the interactive end bead of the small particle chains;  $\sigma = \sigma_{\text{large}} + \sigma_{\text{int. bead}}$ , the sum of the radii of the large particle

and the interactive bead;  $\varepsilon$  is a (positive valued) parameter that determines the strength of an individual large particle-interactive bead interaction; and  $\sigma_{\text{gauss}}$  is a parameter that determines the range of an individual interaction. As usual, the WCA potential is cut off at  $2^{1/6}\sigma$  and shifted such that  $U$  is zero at the cutoff, that is  $U_{\text{WCA}}(r = 2^{1/6}\sigma) = 0$ . The value for  $r_{\text{cutoff}}$  was selected such that  $U(r)$  has safely decayed to near zero. We also used the HOOMD-blue `xplor` option which adds a subtle smoothing near  $r_{\text{cutoff}}$  such that the  $U_{\text{Gaussian}}$  decays smoothly to zero.<sup>1</sup>

These parameters can be adjusted such that the system resembles interactions between two species of colloids of choice. Parameters that can also vary are: particle size, number of chains on each small particle, temperature, system composition (ratio of small:large colloids in the simulation box), and length and stiffness of the chains on the small particles. The properties chosen for the study in this paper are listed in the next section.

## Parameters used for this study

**Table 1:** Parameters used in the present study. **(a)** Fixed parameters ( $\sigma$  is radius). With these, the system resembles a binary system of weakly interacting chain-grafted colloids. **(b)** Variable parameters. Changing these allows us to explore properties of the system.

(a)	(b)		
Parameter	Value	Parameter	Value
$\sigma_{\text{large particle}}$	10.5 nm	small:large particle ratio	6:1
$\sigma_{\text{small particle center}}$	1.0 nm	final lattice	BCC
$\sigma_{\text{chain bead}}$	1.0 nm	temperature	$0.8\text{-}2 k_B T$
$\sigma_{\text{interactive chain end bead}}$	0.5 nm	# chains/small particle	4, 6, 8, 10
$\varepsilon$	$70 k_B T$		
$\sigma_{\text{gauss}}$	4.8 nm		
$r_{\text{cutoff}}$	8.4 nm		
# non-interactive beads/chain	3		

We chose parameters for the size and interaction of our colloids to resemble a system in which the ends of the small chains interact weakly with the large particles, roughly

<sup>1</sup>See `md.pair.pair` documentation:  
<https://hoomd-blue.readthedocs.io/en/stable/module-md-pair.html>

similar to the interaction of single-stranded DNA "sticky" ends in binary systems of DNA-functionalized gold nanoparticles in,<sup>9,23,24</sup> if the size of the large particle is taken to represent the size of the gold core and most of the dense DNA shell. The parameters used are listed in Table 1. With these parameters, at  $T^* = 1$ , the potential well shown in Figure 1B (-4.1 energy units) has a depth of  $-4.1 k_B T$ , which is approximately the binding energy of a single-stranded DNA (3 - 6  $k_B T$ <sup>25,26</sup>). For the parameters we have chosen, the system arranges itself such that the large particles make up a BCC lattice and the small particles are localized at interstitial sites or delocalized.

For this study, we ran using the parameters in Table 1. Specifically, we looked only at a 6:1 small:large particle ratio in the temperature range 0.8 - 2. The reason for choosing a 6:1 ratio will be discussed in Section 6:1 systems form BCC lattices with small particles localized at tetrahedral sites. Within chosen temperature range, we see a transition from localized to delocalized states of the small particles. Because we wanted to understand the nature of this transition as a function of interaction strength and temperature, we report results for a variety of chains per small particle, as well: 4, 6, 8, and 10 chains/small particle.

The simulation was run in HOOMD-blue, version 2.5.1,<sup>27,28</sup> in the NPT ensemble with periodic boundary conditions at near-zero pressure (207 Pa, which is  $\sim 2\%$  of atmospheric pressure). Using a pressure very close to zero enables us to attribute the observed crystal assembly to the interactions between colloids, rather than an external pressure.<sup>9</sup> Additionally, during the NPT portion of the run, the box was allowed to fluctuate in size and shape, which enabled lattices that started in one crystal structure to relax into another if it was favorable to do so.

The full simulation scheme is as follows: we started the simulations under given conditions in multiple initial lattice configurations (BCC, SC, FCC, BCT) with 6x6x6 unit cells in the simulation box. The simulations were then equilibrated, thermalized, and depressurized to their final pressure. This initial sequence lasted 312 ns. Then, the simulations were run in the NPT ensemble for an additional 8.44  $\mu$ s. For analysis, the first 1.38  $\mu$ s were considered to

be an equilibration period and not included in calculation of properties. Therefore, analysis of the simulations was conducted on the last  $7.37 \mu\text{s}$ .

System topology for the simulation was built using Hoobas,<sup>29</sup> analysis was done in Python using the help of MDAnalysis<sup>30,31</sup> and in R, visualization of the simulation in VMD<sup>32</sup> with the GSD plugin<sup>2</sup> using the internal Tachyon ray-tracing library<sup>33</sup> (see Figure 1A), and 3-dimensional scientific plotting and calculation of isosurfaces and 3D densities (see Figures 3 and 6) was done in Mayavi.<sup>34</sup>

## Theoretical free energy of the exact soluble model

The theoretical model described in the main text is derived from calculating the energetic environment of one interactive bead (shown in orange in Figure 1A) and a fixed BCC lattice of large particles (shown in teal in the same figure), in one BCC unit cell. That is, as noted above:

$$Z(a, T) = \int \int e^{-U_{\text{end}}(\vec{r}, \vec{p}; a)/k_B T} d\vec{r} d\vec{p}$$

$$Z(a, T) = (2\pi m k_B T)^{3/2} \int e^{-U_{\text{potential}}(\vec{r}, \vec{p}; a)/k_B T} d\vec{r} \quad (4)$$

where  $\vec{r}$  is integrated over one unit cell and  $d\vec{p}$  is integrated over all real numbers (this Gaussian integral also shows up in the ideal gas partition function and its solution is shown here). The integral has been simplified using the definition of energy as:

$$U_{\text{end}}(\vec{r}, \vec{p}; a) = \frac{\vec{p}^2}{2m} + U_{\text{potential}}(\vec{r}, \vec{p}; a)$$

$$U_{\text{potential}}(\vec{r}, \vec{p}; a) = \sum_n U_{\text{pair}}(|\vec{r} - \vec{R}_n|; a) + \sum_{j < k} U_{\text{WCA}}(|\vec{R}_j - \vec{R}_k|)$$

where  $U_{\text{pair}}(\vec{r}; a)$  is the pair potential between a large particle and an interactive bead, as defined in Equation 1, and the sum is taken over all large particles that are within the

---

<sup>2</sup>See HOOMD-blue GSD plugin for VMD at <https://github.com/mpHoward/gsd-vmd>

cutoff radius of the potential with an interactive bead at  $\vec{r}$  ( $\vec{R}_n$  indicates the position of large particle  $n$ ). In this case, we include 15 large particles: all those pictured in the BCC unit cell in Figure 2A, plus the large particles in the center of all adjacent cells. The range over which  $U_{\text{pair}}(\vec{r}; a)$  is nonzero in this model is short enough such that this captures all interactions.  $U_{\text{WCA}}$  is the WCA potential between large particles; this term becomes important when  $a$  approaches the diameter of the large particles.

We then numerically integrate Equation 4, and can set up any similar equation to calculate any statistical mechanical quantity that can be found with the partition function. For example:

$$\langle U_{\text{int}}(a, T) \rangle = \frac{1}{Z(a, T)} (2\pi m k_B T)^{3/2} \int \left( \sum_n U_{\text{pair}}(|\vec{r} - \vec{R}_n|; a) \right) e^{-U_{\text{potential}}(\vec{r}; a)/k_B T} d\vec{r} \quad (5)$$

The partition function is also used to calculate free energy, as noted above, using:

$$F(a, T) = -k_B T \ln (Z(a, T))$$

This does not include lattice fluctuations, nor does it include a description of the small particles other than as single interactive beads. The lack of lattice fluctuations impact the variance but not the mean of predicted energy values (we have seen this trend when comparing the mean and variances of interaction energy between the fixed and fluctuating lattice cases, as well). Additionally, because the MD model is simple, the pair potentials included are able to capture most of the system's important interactions. Because of that, this model enables us to understand certain energetic interactions and analyze the energy landscape of the system.

This is particularly true when small particles have fewer chains. This is because the small particles interact with 4 large particles when they sit at BCC tetrahedral sites. When there are 4-6 chains on each small particle, the chains, on average, are each attracted to one of the 4 nearby potential wells and therefore, their mutual excluded volume doesn't substantially

impact their average energy values. This is agreement between theory and simulation is stronger for systems with fewer chains per small particle. However, as referred to in the main text (see Figure 2), the bond constraints do matter. These don't allow interactive beads to access the (most energetically favorable) lowest-energy part of the potential wells. However, this appears to simply scale the average energy of the interactive beads, especially, as noted, for systems with fewer chains.

Lastly, note that the lattice parameter and temperature are both inputs to this partition function. It is possible that this formulation could qualitatively predict some lattice expansion; however, because of the differences in average location of the interactive bead between theory and simulation (due to bond constraints), we do not believe that this will be a quantitative prediction for fluctuating properties of a fluctuating lattice simulation. However, this theory can provide a sense of how much the lattice vibrations contribute to properties of a system where they are present.

## Results and discussion

### 6:1 systems form BCC lattices with small particles localized at tetrahedral sites

For each value of chains per small particle, 6:1 systems form BCC lattices over a wide temperature range. At temperatures below this range, we observe formation of other crystal lattice types, and at higher temperatures, we observe liquid or gas phases; see SI for more information on determining BCC stability. Within the BCC range, at lower temperatures the large particles sit at BCC lattice points and the small particles localize at the BCC tetrahedral sites, also known as 12d Wyckoff positions, shown in Figure 2A. The location of the tetrahedral sites means that each small particle can interact with four large particles simultaneously.

An analysis of the symmetry and energy associated with the tetrahedral sites reveals why

small particles localize there. The potential energy of interaction between large particles and the interactive bead at the end of each chain can be seen in Figure 2B. Dark red indicates negative interaction energy, which defines the areas most favorable for the interactive ends to occupy. Conversely, the lighter areas indicate an interaction energy of approximately zero. There are four nearly zero energy sites per face, visible in the (001) plane image in Figure 2B. These are the tetrahedral sites. This suggests that the small particle centers localize at the tetrahedral sites because this enables the interactive ends to access the most energetically favorable regions of the unit cell. Tetrahedral structures have also been observed experimentally. The formation of distorted tetrahedral structures between size asymmetric colloids has been reported within specific size asymmetry ranges,<sup>35</sup> which do not include the dimensions of our system. The experimental tetrahedral clusters, mediated by short ranged but strong potentials (both electrostatic and DNA hybridization), was explained using entropic principles, whereas, here enthalpy seems to be the predominant driving force for the formation of these BCC crystals.

This energy landscape is a good predictor of the locations of particles in simulation. Figure 3A shows the probability density of the small particle centers in a single BCC unit cell at low temperature; they are clearly localized at the tetrahedral sites. Additionally, Figure 2C shows the probability density of the interactive ends in a low temperature simulation; the location of the interactive ends in simulation aligns well with the lowest energy positions in Figure 2B. A notable exception is that the limited reach of the chain in simulation does not allow the interactive beads to reach the bottom of each potential well.

Lastly, the 6:1 ratio between small and large particles allows the tetrahedral sites to be exactly filled. This is because there are 2 lattice points (large particles) and 12 tetrahedral sites (small particles) per BCC unit cell. A lower ratio would produce vacancies in tetrahedral sites; in those cases, we observe hopping of small particles between sites. A larger ratio results in more small particles than available tetrahedral sites; in those cases, interstitial defects are prominent and full localization is not possible. Studying the 6:1 system allows

us to focus on the properties of the localized-to-delocalized transition by avoid confounding factors introduced by vacancy hopping or symmetry change.

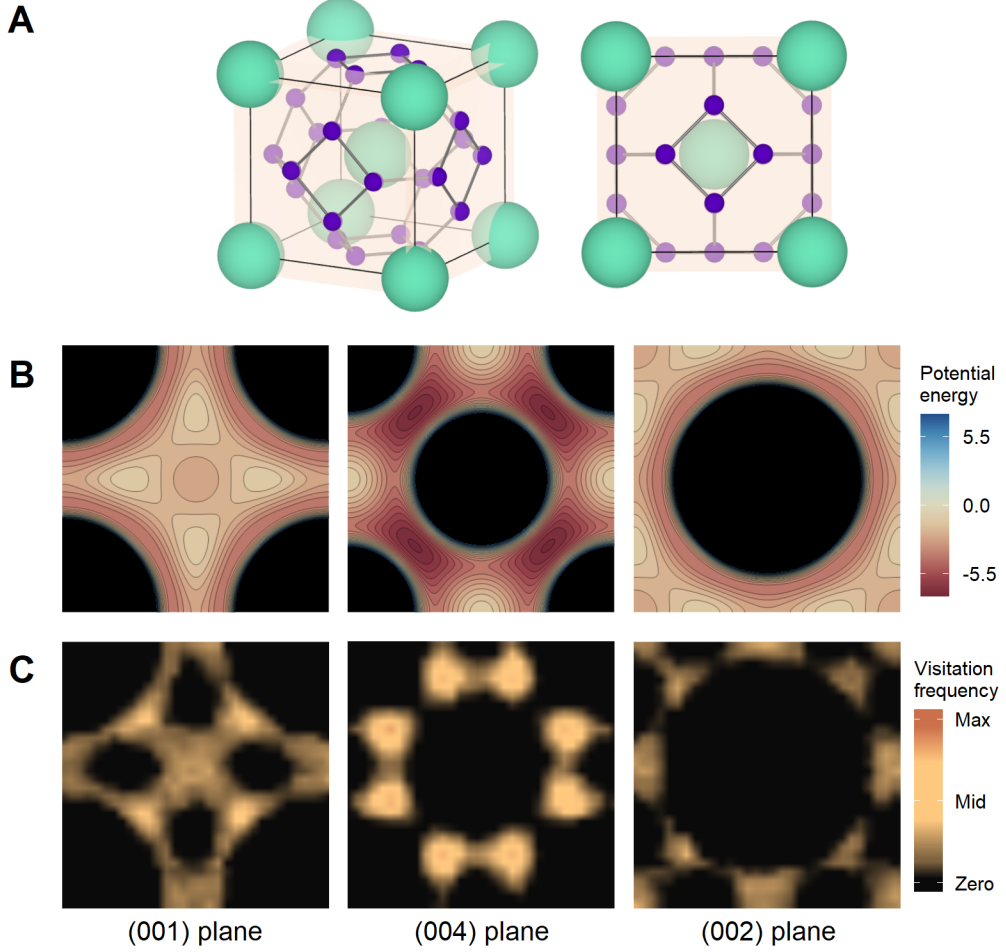


**Figure 2:** (A) BCC lattice sites (turquoise) and tetrahedral interstitial sites (purple) of an ideal BCC lattice. Connections between nearest-neighbor tetrahedral sites are shown as visual guides. (B) Potential energy landscape with respect to one interactive end, based on interaction potential with the large particles, in one BCC unit cell. Deeper red indicates negative values (more favorable energetic interaction), yellow indicates values around zero, and dark blue indicates positive values (unfavorable interactions; the location of large particles is shown in black). (C) Equivalent planes from simulations showing the probability of finding the interactive beads for the case of 6 chains at  $T^* = 0.9$ . Comparing this to (B), interactive bead probability is highest in areas with the most favorable energetic interactions.

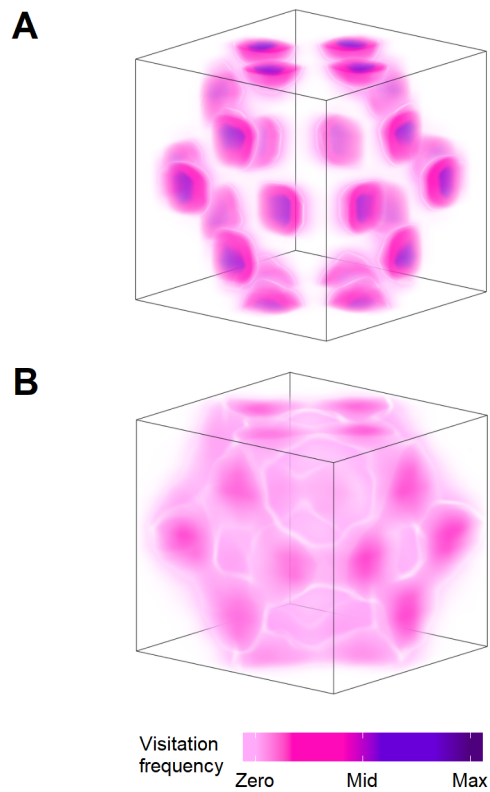


**Figure 3:** Visitation frequency of (centers of) small particles in one unit cell of localized and delocalized systems. Small particles have 6 chains and the maximum of the visitation frequency is 0.0115. **(A)**  $T^* = 0.9$ . Small particles are localized on the tetrahedral sites of the BCC lattice. **(B)**  $T^* = 1.6$ . Small particles are delocalized. They favor the tetrahedral sites of the BCC lattice but also roam around the crystal.

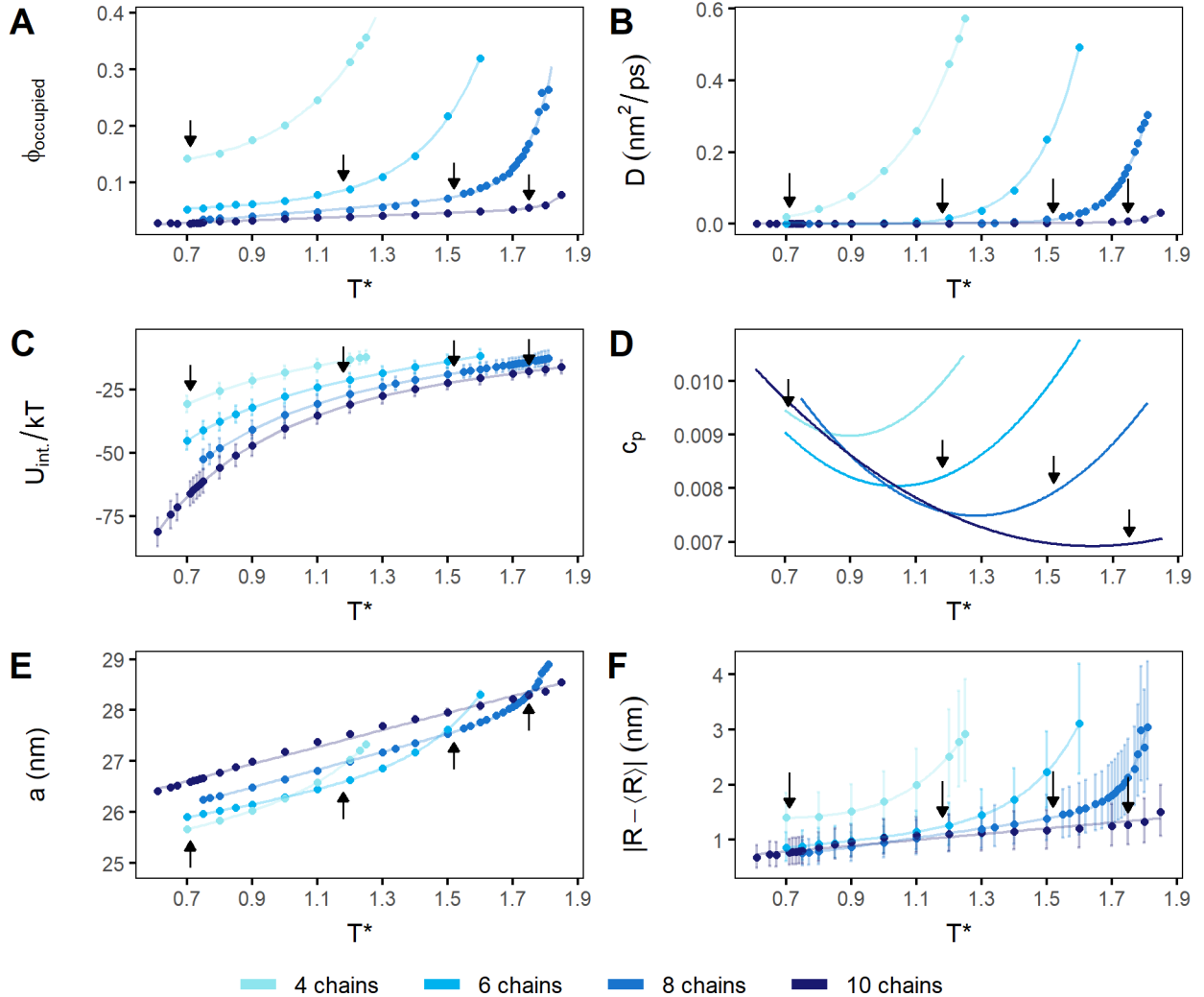


**Figure 4:** Lattice properties as a function of temperature, for all systems studied. Fits are included as visual guides. Black arrows indicate  $T_{\text{deloc}}$ , the onset of delocalization for each system; see SI for how these are identified. Note that all properties change linearly with temperature below and exponentially above  $T_{\text{deloc}}$ , with the exception of  $U_{\text{int.}}$ . **(A)** Approximate volume fraction occupied  $\phi_{\text{occupied}}$  by 70% of the small particles' probability. This is a qualitative measure of delocalization. **(B)** Diffusion constant  $D$  of small particles. **(C)** Average interaction energy between small and large particles  $U_{\text{int.}}$ , per small particle. **(D)** The specific heat at constant pressure  $c_p = C_p/N$  of the system. These curves were calculated by fitting spline curves to mean values of enthalpy and differentiating those curves with temperature. **(E)** Average BCC lattice parameter  $a$ . **(F)** Lattice fluctuations, measured by the median displacement of large particles from their average positions. Uncertainty bars here indicate first and third quartiles, rather than standard deviation, due to the skewed nature of the underlying distribution.

## The localized-to-delocalized transition is smooth and its onset depends on interaction strength

Figure 3 shows the average visitation frequency of the small particle centers in one BCC unit cell, when localized and when delocalized. Though the system pictured has 6 chains per small particle, we see similar behavior for all interaction strengths: when localized, small particles occupy the tetrahedral sites, and when delocalized, they occupy a much larger volume. Even when delocalized, the small particles concentrate around the tetrahedral sites and form a pattern in which the additional volume occupied by the small particles is roughly along the edges of the BCC’s Wigner-Seitz cell. This permits the small particles to move between nearest tetrahedral sites along an energetically-favorable path, equidistant to multiple neighboring lattice points.

We observe a smooth change from localized to delocalized behavior in all cases. Both the onset of delocalization  $T_{\text{deloc}}$  and the overall melting temperature of the lattice  $T_{\text{melt}}$  occur at higher temperatures when the small-large particle interaction is stronger, *i.e* more chains per small particle; see Table S1. Additionally,  $T_{\text{deloc}}$  approaches  $T_{\text{melt}}$  with increasing interaction strength, and this enables us to observe a range of behavior. With 4 chains per small particle (the weakest interaction),  $T_{\text{deloc}}$  is very low, and the sublattice is delocalized at almost every reported temperature. With 6 and 8 chains per small particle,  $T_{\text{deloc}}$  is higher and the system is localized at low temperatures and delocalized at high temperatures. With 10 chains per small particle,  $T_{\text{deloc}}$  is almost equal to  $T_{\text{melt}}$  and the small particles exhibit almost no sublattice delocalization until just before crystal melting.

In Figure 4, we plot the structural and thermodynamic properties of the crystals to characterize their transition. These properties and their importance are listed below.

- Occupied volume fraction of the small particles,  $\phi_{\text{occupied}}$  (Figure 4A), is a qualitative metric that directly measures delocalization. It represents the approximate volume occupied by 70% of the small particles’ probability, as a fraction of the total available

volume (see Supplementary Information for more information). In a previous study,<sup>9</sup> delocalization was quantified using metallicity, a parameter associated to the Shannon entropy of the sublattice. Here we use a more physical parameter associated to the filling of space by small particles in the sublattice.

- Diffusion coefficient of the small particles,  $D$  (Figure 4B), has been used to categorize the order of superionic transitions.<sup>10</sup> Additionally, we have observed that the localized-to-delocalized change is associated with static properties like  $\phi_{\text{occupied}}$  and dynamic properties like  $D$ .
- Average interaction energy of a small particle,  $U_{\text{int}}$  (Figure 4C), is capable of reflecting structural changes.
- Specific heat capacity,  $c_p$  (Figure 4D), provides insight into the order of phase transitions.
- Lattice parameter,  $a$ , (Figure 4E), had been shown to reflect a first order phase transition in previous work in charged colloidal systems.<sup>13</sup>
- Median lattice fluctuations (Figure 4F), are essential for quantifying melting as documented through the Lindemann criterion.

All properties are plotted as a function of reduced temperature  $T^*$ , the value of  $k_B T$  in energy units. In each panel in Figure 4, a black arrow indicates the approximate  $T_{\text{deloc}}$  for each system. This temperature is estimated from the diffusion properties of the sublattice; see SI for more information about how this was calculated.

Many of the properties in Figure 4 exhibit two trends, one during and another before delocalization. The occupied volume fraction  $\phi_{\text{occupied}}$ , diffusion coefficient of the small particles  $D$ , the lattice parameter  $a$ , and the lattice fluctuations (Figures 4A, 4B, 4E, and 4F) all increase linearly below  $T_{\text{deloc}}$  and exponentially above, until the lattice melts. These phenomena appear correlated; particles begin to diffuse and start to occupy a larger volume

at the same temperatures, which is also when lattice expansion and fluctuation begin to increase dramatically. These ties will be explored in later sections.

The smooth increase in  $\phi_{\text{occupied}}$ ,  $a$ , and other properties suggests that the change from localized to delocalized small particles is not a phase transition. This is corroborated by the behavior of the specific heat of the system,  $c_p$ , shown in Figure 4D. We observe that  $c_p$  of all systems is continuous and convex, indicating that no phase transition occurs during the process of delocalization. This is expected because the change from localization to delocalization does not reflect a change in the BCC symmetry imposed by the large particles, nor is the small particles' energy landscape qualitatively impacted.

Even though the  $c_p$  curves do not exhibit evidence of a phase transition, they provide information about the underlying energy landscape of the system. We explain the convexity of the  $c_p$  curves by deactivation and activation of degrees of freedom into which energy can be distributed. The low temperature negative slope of these curves relates to the flattening of the local minima of the energy landscape. This flattening causes a loss of interactive ends' phase space configurations, decreasing  $c_p$ . This is also why the slope is more negative for systems with higher interaction strength. At higher temperatures, new energy modes are enabled in the form of diffusion of the small particles and lattice vibrations. This eventually leads to delocalization, and  $c_p$  continues to increase until the lattice fully melts.

Notably, while the  $\phi_{\text{occupied}}$  and  $a$  change rapidly above  $T_{\text{deloc}}$ , the interaction energy does not. Figure 4C shows the average "binding energy" (the energy of interaction between the large particles and interactive ends, relative to when they are infinitely far apart) per small particle in the system as a function of temperature. That this quantity increases only linearly even above  $T_{\text{deloc}}$  indicates that entropy plays an important role in delocalization. This will be discussed in Section "Vibrational entropy drives lattice expansion."

## Lattice fluctuations are essential for delocalization

To determine the importance of lattice fluctuations to delocalization, we ran additional simulations in which the large particles were fixed on their lattice points and not allowed to vibrate. The lattice parameter used for a given "fixed lattice" run was the mean value calculated from the unconstrained simulation with the same temperature and number of chains per small particle (Figure 4E). We found that without lattice vibrations, the small particles are not able to fully delocalize, which can be seen in the average visitation frequency plots in Figure 6. This is quantified by a large reduction in occupied volume fraction and a slight decrease of the diffusion coefficients. This is similar to the finding by Schommers,<sup>11</sup> who only saw diffusion in molecular dynamics models of superionic  $\alpha$ -AgI when the iodine ion lattice was allowed to vibrate.

Based on these results, delocalization is driven by both lattice vibrations and diffusion. We posit that vibration-driven delocalization occurs when lattice deformation either shifts the energy landscape sufficiently such that small particles can more easily spread out, or that large particles pull small particles between tetrahedral sites while vibrating. Vibration-driven delocalization is fully suppressed in the fixed lattice simulations; this can be seen in Figure 5A. However, some delocalization remains due to small particle diffusion. As can be seen in Figure 5B, diffusion is still present in the fixed lattice simulations and appears to primarily depend on temperature and lattice parameter, which in turn defines the flatness of the energy landscape (Figure 2B).

Analysis of the fixed lattice simulations demonstrates that delocalization is fully achieved only when both lattice vibrations and diffusion are present. The similarity between  $c_p$  curves for the fixed and fluctuating lattice runs, shown in Figure 5D for the 4 chain system, underscores the importance of diffusion. With or without lattice vibrations,  $c_p$  is continuous but not convex. Both  $c_p$  curves exhibit an initial decrease characteristic of the flattening of the energy landscape but differ at higher temperatures. This is due to the lack of lattice vibrations in the fixed lattice simulations. As stated in the previous section, energy modes

associated to the lattice vibrations are what effectively drive the increase of  $c_p$  after the flattening of the energy landscape. Therefore,  $c_p$  for the fixed lattice simulations continues to decrease, whereas, the unconstrained simulations'  $c_p$  increases.

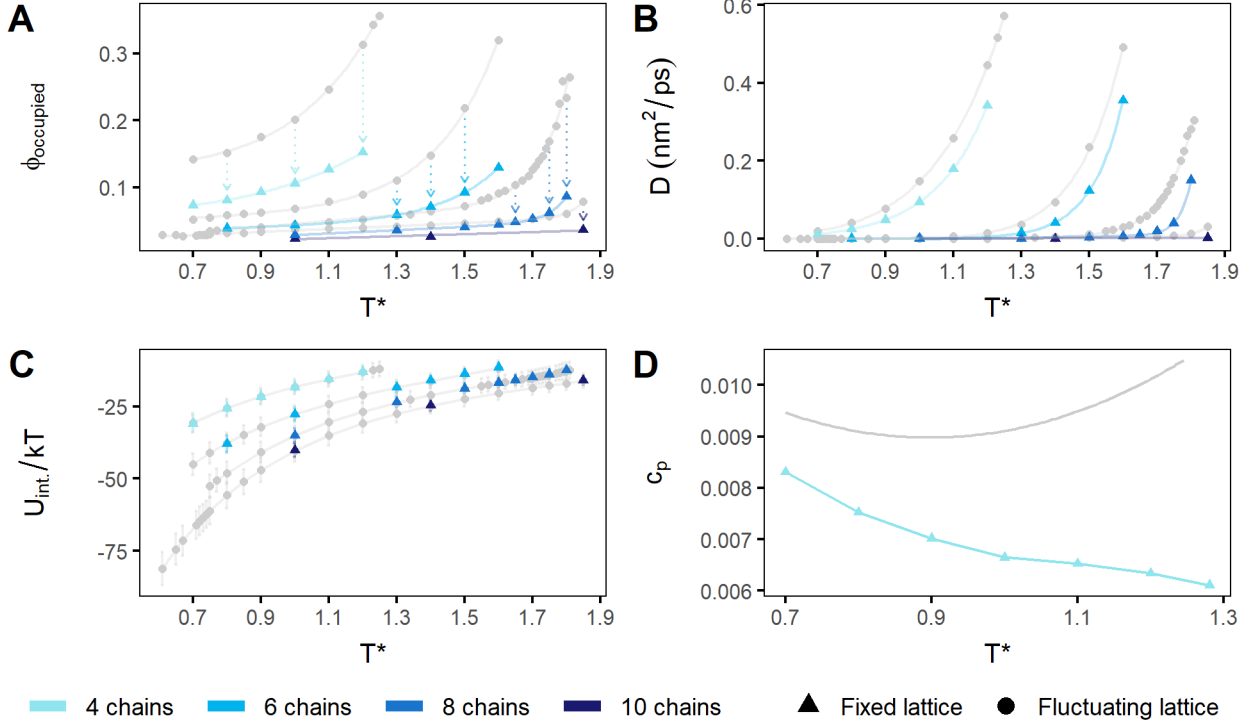


**Figure 5:** Lattice properties as a function of temperature, for fixed lattice runs and compared to unconstrained runs. Data from the main runs (also in Figure 4) is shown in grey circles and data from the fixed lattice runs is shown in blue triangles. Removing lattice fluctuations substantially suppresses delocalization and minorly suppresses diffusion. **(A)** Approximate occupied volume fraction  $\phi_{\text{occupied}}$ . Arrows connect fixed and fluctuating lattice simulations with the same number of chains per small particle. **(B)** Diffusion constant  $D$  of small particles. **(C)** Average interaction energy  $U_{\text{int}}$  of small particles with large particles. Because corresponding fixed and fluctuating lattice runs have the same average lattice constant, the average interaction energy of the small particles does not change, though the fluctuations do. **(D)** The specific heat at constant pressure  $c_p$  of the system with 4 chains per small particle.

## Vibrational entropy drives lattice expansion

Having established that lattice vibrations are crucial for delocalization, we turn to address the exponential expansion shown in Figure 4E. The exponential lattice expansion appears

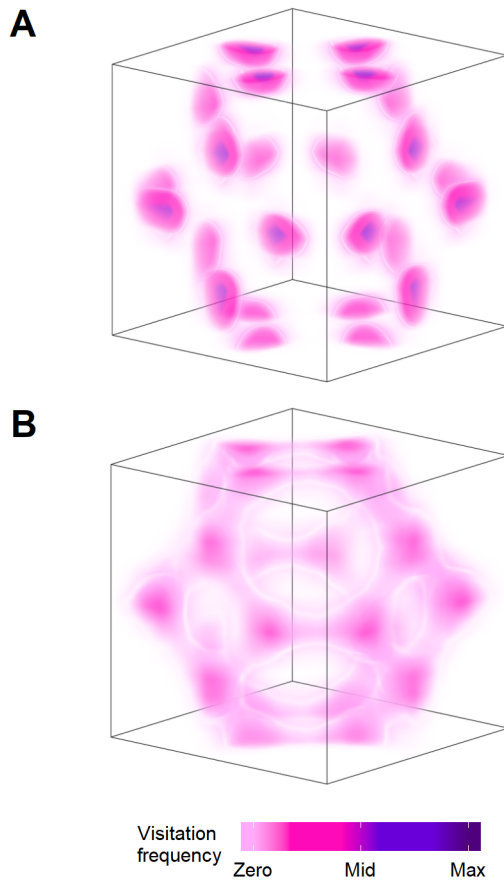


**Figure 6:** The average visitation frequency of the small particle centers in a fixed lattice system with 6 chains per small particle. The maximum of the visitation frequency is 0.0250. Without lattice fluctuations, the small particles in the delocalized case occupy less volume than when lattice fluctuations are present. Note that the unit cells of these lattices are actually different sizes, but the images have been scaled such that the two are comparable. (A)  $T^* = 0.9$ . Small particles are localized on the tetrahedral sites of the BCC lattice. This is similar to the unconstrained lattice case. (B)  $T^* = 1.6$ . Small particles are delocalized. Again, they favor tetrahedral sites but also diffuse between sites. This delocalization is more coherent than in the fluctuating lattice case.

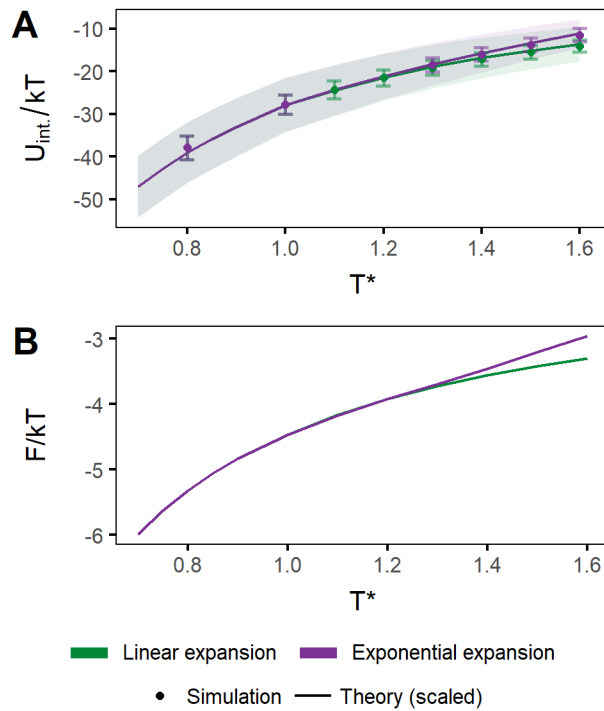


**Figure 7:** Comparison between theory and simulation (6 chain system). **(A)** Interaction energy between small and large particles. Line represents scaled theory results; points represent simulation results. **(B)** Theoretical prediction of the free energy of the systems with exponentially expanding lattice (main cases) and linearly expanding lattice. The free energy of the linear case is lower, indicating that something outside the theory must explain why the lattice expands exponentially.

to be highly correlated with delocalization, but the reason that it occurs is unclear. To gain a better understanding, we performed a free energy analysis of our system using the same simplified theoretical model that predicted the energy landscape of a BCC unit cell in Figure 2B. This theoretical model describes one interactive end in a fixed (non-fluctuating) BCC unit cell of large particles. The energy of one lattice configuration based on the temperature, lattice parameter, and position of the interactive end  $U_{\text{end}}(\vec{r}, \vec{p}; a)$  is found in Equation 5, and is based on Equation 1 and Figure 1A. Using these definitions and  $a$  and  $T$  from simulation, we calculated the partition function  $Z(a, T) = \int e^{-U_{\text{end}}(\vec{r}, \vec{p}; a)/k_B T} d\vec{r} d\vec{p}$  by numerically integrating over a unit cell. From this, we could calculate all relevant thermodynamic properties. See the Methods Section for more information.

We employed this model to explain why the lattice expands so rapidly at the onset of delocalization. To do this, we compared two cases: *(i)* exponential expansion, which is the observed behavior of the lattice, and *(ii)* linear expansion, in which the lattice expands linearly over the entire temperature range. We ran fixed lattice simulations of both cases and compared those to theory.

Figure 7A shows the average interaction energy per small particle in the exponentially and linearly expanding cases, for both simulation (points) and theory (solid line). We find that the theoretical model accurately predicts the energy in both cases up to a multiplicative factor. In the theoretical model, the interactive energy of a single interactive end is  $\langle U_{\text{int}} \rangle = \frac{1}{Z(a, T)} \int U_{\text{int}}(\vec{r}; a) e^{-U_{\text{end}}(\vec{r}, \vec{p}; a)/k_B T} d\vec{r} d\vec{p}$ . Because the result of this integral is the potential energy of one interactive end, we multiply  $\langle U_{\text{int}} \rangle$  by the number of chains per small particle to estimate the total energy of a small particle. For example, Figure 7 shows simulation results for runs with 6 chains per small particle. If the theoretical model was exact, we would multiply  $\langle U_{\text{int}} \rangle$  by 6. However, the theoretical model overestimates the average energy per small particle relative to simulation. This is due to the fact that, in simulation, the limited reach of the chains does not allow the interactive end to fully explore the lowest energy portions of the potential well (this can be seen in the comparison between Figures 2B and 2C).

The result is that the interactive end's energy is about 20% lower in simulation than in theory. Therefore, the theoretical results shown in Figure 7A are scaled by a factor of 0.82 (this factor differs by a few percent for the case of 4 chains per small particle). Additionally, excluded volume interactions of densely grafted particles can impact the possible configurations of those particles. This effect is not observed for small particles with 4 and 6 chains, because the average energy per chain is independent of the number of chains. Meanwhile, excluded volume interactions affect particle energy to a minor extent in systems with 8 and 10 chains per small particle.

The close correspondence between small particle potential energy in simulation and that predicted by theory indicates that the theoretical model can predict differences in properties between the exponentially and linearly expanding cases. Therefore, we used this model to compare the free energies of the two cases, to understand why one is favorable. Using the partition function, we calculated the Helmholtz free energy,  $F = -k_B T \ln Z$ , which is plotted in Figure 7B. According to the theoretical model, the free energy of the linearly expanding lattice should be *lower* than the free energy of the exponentially expanding lattice, so exponential expansion should be not favorable. We conclude, therefore, that at least one of the few interactions missing from the theoretical model must be what drives the observed exponential expansion. There are three elements missing from the theoretical model: *(i)* excluded volume interactions due to the presence of the other particle types, *(ii)* bond constraints, and *(iii)* lattice vibrations. We have already established that excluded volume interactions do not greatly impact the average energy of the small particles. Therefore, excluded volume should not contribute to the difference between the exponentially and linearly expanding cases, especially with 4 and 6 chains per small particle. We also can account for the bond constraints by scaling the potential energy by about 0.8, as mentioned above. Additionally, bond constraints limit the reach of the interactive ends and therefore are likely to make rapid lattice expansion less energetically favorable. It must be vibrational entropy that drives the exponential lattice expansion. Additionally, large lattice fluctuations have already been seen

to stabilize BCC crystals around its melting temperature<sup>36</sup> mostly due to its non close packed structure (or low coordination number). Vibrational entropy becomes dominant only above a certain temperature that depends on the number of chains per small particle. This is why we see exponential expansion and delocalization at different temperatures depending on the interaction strength. Based on this analysis, we can see that lattice vibrations determine both the degree of delocalization and the thermal expansion of the lattice.

## Conclusion

In summary, we have seen that the localized-to-delocalized transition of 6:1 binary colloidal systems is continuous, dominated by lattice entropy also as known as lattice vibrations, and tunable by number of chains per small particle (interaction strength). Our results suggest that the delocalization of the sublattice is not a phase transition, given that there is no accompanying symmetry change because the crystal remains a BCC lattice and small particles still favor tetrahedral sites. The lack of a phase transition is evidenced by the fact that  $c_p$  is continuous for all systems. A continuous transition has also been reported for some superionic crystals.<sup>37</sup> Moreover, delocalization is also highly tied to vibrational entropy. Using simulations in which lattice vibrations were prohibited, as well as a free energy analysis using a simplified theoretical model, we conclude that most delocalization is driven by lattice vibrations, and that vibrational entropy is what causes the lattice to expand so rapidly above  $T_{\text{deloc}}$ . We can also see that the presence of the localized-to-delocalized transition is dependent on the number of chains per small particle, a proxy for interaction strength. The nature of the transition does not change as the number of chains per small particle does; however, too many chains suppress delocalization almost entirely.

Based on this analysis, in order to observe sublattice delocalization in a binary colloidal system, small particle diffusion and sufficient lattice vibration must be present. Our findings show this can occur with a binding energy per chain of  $\sim 3 - 5 k_B T$  and a reach of chains

or interactions of about one quarter to one third of the estimated lattice parameter. Per Figure 4C, delocalization occurs when the total interaction energy is around and above 25  $k_B T$ /particle, spread out between chains. This can be tuned by the number of chains grafted to the small particles. The validation between the theoretical model and simulation results reveals that the potential energy landscape of a single interactive end within a BCC unit cell is a faithful representation of the simulated system, even though we have excluded the existence of other particles within the theoretical model. This representation is accurate because of the larger range of attraction between the large particles and the interactive ends compared to the range of repulsion between interactive ends. Additionally, we posit that, for the possibility of delocalization, the small particle size must be comparable to the fluctuations of the lattice and an asymmetry of interaction ranges must exist. This can also be achieved with charged colloids given a disparity in charge magnitudes.<sup>13,38</sup> The attraction range between small and large particles must be greater than the repulsion range between small particles because small particles must sit at and travel between interstitial sites that are closer together than lattice points.

Therefore, similar analysis and conclusions may be obtained in colloidal systems without grafted chains, but with certain caveats. For example, the energy landscape may induce discontinuities within certain physical parameters like the lattice constant<sup>13</sup> given the existence of local and global minima in the energy landscape. This would enable the occupation of different symmetry sublattice positions associated with these local energy minima by the delocalized species.<sup>14</sup> This would impact the internal energy of the crystal. Thus, complex energy landscapes may nullify our claims of a non phase transition from localized to delocalized behavior.

Another main ingredient needed for delocalization of the sublattice exhibited resembles that reported for superionic materials.<sup>14,15</sup> Soft vibrational modes, which are high amplitude vibrations, are reported to be important for the presence of conduction of the mobile species, most commonly a cationic interstitial within a mostly anionic lattice. Soft vibrational modes

are stabilized by non close packed crystals, also seen in superionics.<sup>14,15</sup> The mechanism of this phenomenon is still not fully understood in superionic materials. But with the use of our results, it is possible that the electron density may have a similar role in the stability of the crystal as that of the potential energy landscape of our system. Comparing the two may be done by assuming partial ionic bonds between the static and mobile species. If true, then our findings using these colloidal systems would translate to superionic materials which are relevant to applications for the improved design of solid-state batteries for energy storage.<sup>39-41</sup>

## Supporting Information Available:

Information concerning the temperature ranges and evolution of the pair distribution functions over the temperature range of the BCC lattices are detailed. The determination of  $T_{\text{deloc}}$  is discussed, the calculation method for occupied volume and the heat capacity is detailed. The evolution of the unique interacting pairs between a small particle and large particles is also quantified for all systems (PDF). Videos of rotating unit cells of a localized and delocalized sublattice for both types of simulations, fixed and unconstrained/free lattices (.mp4 videos).

## Acknowledgement

This work was supported by the Center for Bio-Inspired Energy Science, an Energy Frontier Research Center funded by the US Department of Energy, Office of Science, Basic Energy Sciences under Award DE-SC0000989. H.L.-R. thanks a fellowship from Fulbright-Garcia Robles and A.E. thanks a fellowship from the National Science Foundation under grant DGE-1450006. M.O.d.l.C. thanks the computational support of the Sherman Fairchild Foundation.

## References

1. Shevchenko, E. V.; Talapin, D. V.; Kotov, N. A.; O'Brien, S.; Murray, C. B. Structural diversity in binary nanoparticle superlattices. *Nature* **2006**, *439*, 55–59.
2. Hynninen, A. P.; Christova, C. G.; Van Roij, R.; Van Blaaderen, A.; Dijkstra, M. Prediction and observation of crystal structures of oppositely charged colloids. *Physical Review Letters* **2006**, *96*, 138308.
3. Bodnarchuk, M. I.; Kovalenko, M. V.; Heiss, W.; Talapin, D. V. Energetic and Entropic Contributions to Self-Assembly of Binary Nanocrystal Superlattices: Temperature as the Structure-Directing Factor. *Journal of the American Chemical Society* **2010**, *132*, 11967–11977.
4. Hueckel, T.; Hocky, G. M.; Palacci, J.; Sacanna, S. Ionic solids from common colloids. *Nature* **2020**, *580*, 487–490.
5. Oh, J. S.; Yi, G. R.; Pine, D. J. Reconfigurable Self-Assembly and Kinetic Control of Multi-programmed DNA-Coated Particles. *ACS Nano* **2020**, *14*, 4595–4600.
6. Leunissen, M. E.; Christova, C. G.; Hynninen, A.-P.; Royall, C. P.; Campbell, A. I.; Imhof, A.; Dijkstra, M.; Van Roij, R.; Van Blaaderen, A. Ionic colloidal crystals of oppositely charged particles. *Nature* **2005**, *437*, 235–240.
7. Filion, L.; Hermes, M.; Ni, R.; Vermolen, E. C.; Kuijk, A.; Christova, C. G.; Stiefelhagen, J. C.; Vissers, T.; Van Blaaderen, A.; Dijkstra, M. Self-assembly of a colloidal interstitial solid with tunable sublattice doping. *Physical Review Letters* **2011**, *107*, 168302–1–168302–4.
8. Van Der Meer, B.; Lathouwers, E.; Smallenburg, F.; Filion, L. Diffusion and interactions of interstitials in hard-sphere interstitial solid solutions. *Journal of Chemical Physics* **2017**, *147*, 234903.

9. Girard, M.; Wang, S.; Du, J. S.; Das, A.; Huang, Z.; Dravid, V. P.; Lee, B.; Mirkin, C. A.; Olvera de la Cruz, M. Particle analogs of electrons in colloidal crystals. *Science* **2019**, *364*, 1174–1178.

10. Hull, S. Superionics: crystal structures and conduction processes. *Reports on Progress in Physics* **2004**, *67*, 1233.

11. Schommers, W. Correlations in the Motion of Particles in n-Agl: A Molecular-Dynamics Study. *Physical Review Letters* **1977**, *38*, 1536–1539.

12. Tatsumisago, M.; Shinkuma, Y.; Minami, T. Stabilization of superionic  $\alpha$ -Agl at room temperature in a glass matrix. *Nature* **1991**, *354*, 217–218.

13. Lin, Y.; Olvera de la Cruz, M. Sublattice melting in binary superionic colloidal crystals. *Physical Review E* **2020**, *101*, 032603.

14. Wang, Y.; Richards, W. D.; Ong, S. P.; Miara, L. J.; Kim, J. C.; Mo, Y.; Ceder, G. Design principles for solid-state lithium superionic conductors. *Nature Materials* **2015**, *14*, 1026–1031.

15. Muy, S.; Bachman, J. C.; Giordano, L.; Chang, H. H.; Abernathy, D. L.; Bansal, D.; Delaire, O.; Hori, S.; Kanno, R.; Maglia, F.; Lupart, S.; Lamp, P.; Shao-Horn, Y. Tuning mobility and stability of lithium ion conductors based on lattice dynamics. *Energy and Environmental Science* **2018**, *11*, 850–859.

16. Donakowski, M. D.; Godbe, J. M.; Sknepnek, R.; Knowles, K. E.; Olvera de la Cruz, M.; Weiss, E. A. A Quantitative Description of the Binding Equilibria of para-Substituted Aniline Ligands and CdSe Quantum Dots. *The Journal of Physical Chemistry C* **2010**, *114*, 22526–22534.

17. Harris, R. D.; Amin, V. A.; Lau, B.; Weiss, E. A. Role of interligand coupling in de-

terminating the interfacial electronic structure of colloidal CDS quantum dots. *ACS Nano* **2016**, *10*, 1395–1403.

18. Kalsin, A. M.; Fialkowski, M.; Paszewski, M.; Smoukov, S. K.; Bishop, K. J.; Grzybowski, B. A. Electrostatic self-assembly of binary nanoparticle crystals with a diamond-like lattice. *Science* **2006**, *312*, 420–424.
19. Klajn, R.; Bishop, K. J.; Grzybowski, B. A. Light-controlled self-assembly of reversible and irreversible nanoparticle suprastructures. *Proceedings of the National Academy of Sciences of the United States of America* **2007**, *104*, 10305–10309.
20. Zhang, J.; Santos, P. J.; Gabrys, P. A.; Lee, S.; Liu, C.; Macfarlane, R. J. Self-Assembling Nanocomposite Tectons. *Journal of the American Chemical Society* **2016**, *138*, 16228–16231.
21. Santos, P.; J.; Cao, Z.; Zhang, J.; Alexander-Katz, A.; Macfarlane, R. J. Dictating Nanoparticle Assembly via Systems-Level Control of Molecular Multivalency. *Journal of the American Chemical Society* **2019**, *141*, 14624–14632.
22. Santos, P. J.; Cheung, T. C.; Macfarlane, R. J. Assembling Ordered Crystals with Disperse Building Blocks. *Nano Letters* **2019**, *19*, 5774–5780.
23. Knorowski, C.; Burleigh, S.; Travesset, A. Dynamics and statics of DNA-programmable nanoparticle self-assembly and crystallization. *Physical Review Letters* **2011**, *106*, 215501.
24. Li, T. I.; Sknepnek, R.; MacFarlane, R. J.; Mirkin, C. A.; Olvera De La Cruz, M. Modeling the crystallization of spherical nucleic acid nanoparticle conjugates with molecular dynamics simulations. *Nano Letters* **2012**, *12*, 2509–2514.
25. Biancaniello, P. L.; Kim, A. J.; Crocker, J. C. Colloidal Interactions and Self-Assembly using DNA Hybridization. *Physical Review Letters* **2005**, *94*.

26. Rogers, W. B.; Crocker, J. C. Direct measurements of DNA-mediated colloidal interactions and their quantitative modeling. *Proceedings of the National Academy of Sciences of the United States of America* **2011**, *108*, 15687–15692.

27. Anderson, J. A.; Lorenz, C. D.; Travesset, A. General purpose molecular dynamics simulations fully implemented on graphics processing units. *Journal of Computational Physics* **2008**, *227*, 5342–5359.

28. Glaser, J.; Nguyen, T. D.; Anderson, J. A.; Lui, P.; Spiga, F.; Millan, J. A.; Morse, D. C.; Glotzer, S. C. Strong scaling of general-purpose molecular dynamics simulations on GPUs. *Computer Physics Communications* **2015**, *192*, 97–107.

29. Girard, M.; Ehlen, A.; Shakya, A.; Bereau, T.; Olvera de la Cruz, M. Hoobas: A highly object-oriented builder for molecular dynamics. *Computational Materials Science* **2019**, *167*.

30. Michaud-Agrawal, N.; Denning, E. J.; Woolf, T. B.; Beckstein, O. MDAnalysis: A toolkit for the analysis of molecular dynamics simulations. *Journal of Computational Chemistry* **2011**, *32*, 2319–2327.

31. Gowers, R.; Linke, M.; Barnoud, J.; Reddy, T.; Melo, M.; Seyler, S.; Domański, J.; Dotson, D.; Buchoux, S.; Kenney, I.; Beckstein, O. MDAnalysis: A Python Package for the Rapid Analysis of Molecular Dynamics Simulations. *Proceedings of the 15th Python in Science Conference* **2016**, 98–105.

32. Humphrey, W.; Dalke, A.; Schulten, K. VMD: Visual Molecular Dynamics. *Journal of Molecular Graphics* **1996**, *14*, 33–38.

33. Stone, J. E. An Efficient Library For Parallel Ray Tracing And Animation. Ph.D. thesis, Computer Science Department, University of Missouri-Rolla, 1998.

34. Ramachandran, P.; Varoquaux, G. Mayavi: 3D visualization of scientific data. *Computing in Science and Engineering* **2011**, *13*, 40–51.

35. Schade, N. B.; Holmes-Cerfon, M. C.; Chen, E. R.; Aronzon, D.; Collins, J. W.; Fan, J. A.; Capasso, F.; Manoharan, V. N. Tetrahedral colloidal clusters from random parking of bidisperse spheres. *Physical Review Letters* **2013**, *110*, 148303.

36. Sprakel, J.; Zaccione, A.; Spaepen, F.; Schall, P.; Weitz, D. A. Direct Observation of Entropic Stabilization of bcc Crystals Near Melting. *Physical Review Letters* **2017**, *118*, 088003.

37. Salamon, M. B., Ed. *Physics of Superionic Conductors*; Topics in Current Physics; Springer Berlin Heidelberg: Berlin, Heidelberg, 1979; Vol. 15; p Chapter 7.

38. Higler, R.; Sprakel, J. Doping colloidal bcc crystals-interstitial solids and meta-stable clusters. *Scientific Reports* **2017**, *7*, 1–13.

39. Goodenough, J. B.; Park, K.-S. The Li-Ion Rechargeable Battery: A Perspective. *J. Am. Chem. Soc* **2013**, *29*, 31.

40. Bachman, J. C.; Muy, S.; Grimaud, A.; Chang, H. H.; Pour, N.; Lux, S. F.; Paschos, O.; Maglia, F.; Lupart, S.; Lamp, P.; Giordano, L.; Shao-Horn, Y. Inorganic Solid-State Electrolytes for Lithium Batteries: Mechanisms and Properties Governing Ion Conduction. *Chemical Reviews* **2016**, *116*, 140–162.

41. Famprikis, T.; Canepa, P.; Dawson, J. A.; Islam, M. S.; Masquelier, C. Fundamentals of inorganic solid-state electrolytes for batteries. *Nature Materials* **2019**, *18*, 1278–1291.